Structural and electronic properties of Tl films on Ag(111): From $(\sqrt{3}\times\sqrt{3})$ surface alloy to moiré superstructure

Patrick Härtl,[1,*] Sven Schemmelmann,[2,†] Peter Krüger,[3] Markus Donath,[2] and Matthias Bode[1,4]

[1]*Physikalisches Institut, Experimentelle Physik II, Julius-Maximilians-Universität Würzburg, Am Hubland, 97074 Würzburg, Germany*

[2]*Physikalisches Institut, University of Münster, Wilhelm-Klemm-Straße 10, 48149 Münster, Germany*

[3]*Institut für Festkörpertheorie, University of Münster, Wilhelm-Klemm-Straße 10, 48149 Münster, Germany*

[4]*Wilhelm Conrad Röntgen Research Center for Complex Material Systems, Julius-Maximilians-Universität Würzburg, Am Hubland, 97074 Würzburg, Germany*

(Received 10 March 2023; accepted 9 May 2023; published 23 May 2023)

We present a detailed study of the growth behavior and the electronic properties of thin Tl films epitaxially grown on Ag(111). We combine experimental results obtained by Auger electron spectroscopy, low-energy electron diffraction, scanning tunneling microscopy, scanning tunneling spectroscopy (STS), and inverse photoemission (IPE). The electronic properties identified by STS and IPE are substantiated via density functional theory (DFT) calculations. For a Tl coverage of 0.33 atomic layers (AL), our experimental results show the formation of small patches with a $(\sqrt{3}\times\sqrt{3})$ reconstruction. With STS and IPE, we observe two dominant empty-state electronic features at $E - E_F \approx 1.6$ and 3.5 eV, which are attributed to downward dispersing s, p_z-derived states and to states with p_z orbital symmetry, respectively. On the basis of band structure and charge distribution calculations, we discuss the variation of the binding energies of the respective electronic features observed by STS and IPE. Above 0.5 AL, a moiré superstructure evolves due to the rather large lattice mismatch between the Tl adlayer and Ag(111) which exhibits a sharp spectroscopic feature at around $E - E_F \approx 3.1$ eV in STS and IPE. The comparison with DFT calculations suggests that it originates from a predominantly p_z-like surface state. For even larger film thicknesses up to 4 AL, we find a rotation of the Tl layer with respect to the Ag(111) substrate of $\alpha = \pm(2.50 \pm 0.20)^\circ$.

DOI: 10.1103/PhysRevB.107.205144

I. INTRODUCTION

While spin-orbit interaction (SOI) has long been considered as a typically small correction to the energy of electronic states, various SOI-based phenomena which strongly influence the properties of materials have been discovered in the last 20 years. A particularly prominent example is the Rashba effect [1,2] which lifts the spin degeneracy of the electronic states in systems with broken inversion symmetry and results in a momentum-dependent splitting even without requiring an external magnetic field. Originally, the Rashba effect was predicted for semiconductors where inversion symmetry was lifted either by external electric fields [3] or noncentrosymmetric crystal structures [4]. Only later it was realized that a Rashba effect can also be expected for a two-dimensional electron gas at metallic surfaces. Surface-sensitive measurement methods allowed for the experimental confirmation of the Rashba splitting of the Au(111) surface state [5–10], but the strength of the spin-orbit splitting is typically very small with Rashba energies E_R [11] in the meV range.

The induction of huge in-plane potential gradients by means of surface alloys was suggested as a possibility to manipulate and potentially increase E_R [12]. Later, theoretical studies showed a more complex interplay between atomic SOI, potential gradients, and asymmetries of the electron wave functions [13–15] than originally considered. Nevertheless, a class of isostructural surface alloys between heavy transition metals and noble metals such as Cu(111) or Ag(111) surfaces turned out to provide values of the Rashba energies E_R which are two orders of magnitude larger than for Au(111) [12,16–34]. The materials systems studied to date include Bi/Ag(111) [12,16–27,35], Bi/Cu(111) [27–31], Pb/Ag(111) [16–20,32], Sb/Ag(111) [20,28,33,34], and Sb/Cu(111) [28].

The group III post-transition metal thallium (Tl) with the atomic number $Z = 81$ may be another element which could potentially produce a significant Rashba effect when deposited on, for example, a Ag(111) surface. With an electron configuration $6p^1$, Tl possesses one electron less in the valence shell than Pb ($Z = 82$, $6p^2$) and two less than Bi ($Z = 83$, $6p^3$). This reduced valence is associated with a systematic variation of the electronic structure. Both $(\sqrt{3}\times\sqrt{3})$-ordered surface alloys of Pb [16–20,32] and Bi on Ag(111) [12,16–27,35] exhibit two Rashba-split surface states. When going from $BiAg_2$ to $PbAg_2$, two main trends are observed: (i) the Fermi level E_F shifts down by about 800 meV and (ii) the Rashba energy E_R of the s, p_z- and $m_j = 1/2$-derived states decreases from 200 meV for Bi to about 100 meV for Pb. If this trend continues for Tl, one would expect surface states which are energetically located far in the unoccupied regime with Rashba energies of a few tens of meV only—but still significantly higher than on Au(111).

In this paper, using low-energy electron diffraction (LEED) experiments, Auger electron spectroscopy (AES),

*Corresponding author: patrick.haertl@uni-wuerzburg.de

†Corresponding author: sven.schemmelmann@uni-muenster.de

and scanning tunneling microscopy (STM), we study the structural properties of Tl on Ag(111) for submonolayer coverages up to films with a thickness of about 4 AL. For the detection of surface states, with a possible Rashba splitting, scanning tunneling spectroscopy (STS) experiments were performed at cryogenic temperature. Furthermore, the energy-momentum dispersion of unoccupied states is determined by inverse photoemission (IPE). The obtained results are interpreted on the basis of density functional theory (DFT) calculations.

II. EXPERIMENTAL METHODS

The experimental results presented in this paper are based on the expertise of two experimental groups at the universities of Würzburg and Münster. In Würzburg, the STM, STS, LEED, and AES experiments were performed in two different ultrahigh vacuum (UHV) systems. The first UHV system consists of two chambers with base pressures $p < 10^{-10}$ mbar. In one chamber, the Ag(111) substrate can be cleaned by argon ion sputtering, while the other chamber is equipped with the Tl evaporator. Thallium granules (Alfa Aesar, diameter $\leqslant 6$ mm, purity 99.99%) were loaded into a glass crucible and deposited with a home-built thermal evaporator heated radiatively by a W filament onto the clean Ag(111) substrate. Additionally, the chamber is equipped with a four-grid LEED optics which also allows for AES by means of a retarding field energy analyzer. The commercial flow-cryostat variable-temperature (VT)-STM (Omicron Nanotechnology GmbH) allows for measurements at a sample temperature $T_{\text{sample}} = 40$–400 K.

The sample can be heated on a manipulator by a resistive heater or cooled via liquid nitrogen, which allows deposition and LEED/AES measurements in a temperature range between $T_{\text{sample}} = 120$ and 700 K. The sample temperature was measured both by a thermocouple attached to the sample slot and with an optical pyrometer (IMPAC Pyrometer Series 140) via a window with visual access to the sample position. The emissivity was assumed to be $\epsilon = 0.10$.

The second UHV system is a two-chamber setup with a base pressure $p < 10^{-10}$ mbar which is equipped with a low-temperature STM at an operating temperature of $T_{\text{STM}} = 4.9$ K (Omicron Nanotechnology GmbH). In this system, a LEED/AES apparatus (Omicron Nanotechnology GmbH) is also available, but the manipulator cannot be cooled. At both systems, the identical Tl evaporator was used. Topographic STM data were recorded in the constant-current mode of operation at the indicated set-point current I_{set}. Throughout the paper the applied bias voltage will be given as the sample bias U_{bias}. We used electrochemically etched tungsten tips. For STS measurements we added a small modulation (frequency ν) to the bias voltage, U_{mod}. The dI/dU signal was determined by frequency- and phase-sensitive detection with a lock-in amplifier.

Spin- and angle-resolved IPE experiments were performed in Münster in a UHV apparatus with a base pressure of $p < 5\times10^{-11}$mbar. The apparatus consists of three chambers. The preparation chamber is equipped with a sputter gun and a home-built Tl evaporator for sample preparation and with LEED and AES for sample characterization. In a second chamber, spin-polarized electrons are excited from a GaAs-based photocathode with a spin polarization of 29% [36]. The electron beam is guided via an electron optics into the analysis chamber for IPE measurements. The beam incidences the sample at an angle θ with respect to the surface normal and with a beam divergence $\Delta\theta_{\text{FWHM}} \approx 3^\circ$ similar to values in the literature [37]. The emitted photons from transitions into unoccupied electron states are detected by a bandpass detector with a mean detection energy of $\hbar\omega = 9.9$ eV [38] at a photon takeoff angle of 65° in and 32° out of the measuring plane [39]. The overall energy resolution of the IPE experiment is $\Delta E_{\text{FWHM}} \approx 400$ meV [40]. The IPE spectra were obtained at a sample temperature of 300 K.

In all experiments, the Ag(111) substrate was prepared by cycles of argon-ion (Ar^+) bombardment for 10–30 min at $E_{\text{Ar}} = 500$–1000 eV followed by 10–20-min postannealing at $T_{\text{sample}} \approx 770$ K. During the Tl deposition, the substrate was held at a temperature of $T_{\text{sample}} \approx 478$ K which was identified as the optimal substrate temperature for growing highly ordered Tl films (see Supplemental Material [41]). To compare the results in Würzburg and Münster, the LEED images were used as reference [41].

The lattice constant of the fcc crystal structure of the Ag(111) substrate at room temperature amounts to $a^{\text{lit}}_{\text{Ag(111)}} = 289$ pm [44], whereas Tl itself crystallizes in a hcp structure with $a^{\text{lit}}_{\text{Tl}} = 343$ pm [45], resulting in a lattice mismatch of ≈16 %. For the correct interpretation of layer thicknesses, it is insightful to calculate the atomic densities for both materials. For Ag(111) the atomic density $\rho = n/A$, with the number of atoms n per area A, amounts to $\rho_{\text{Ag(111)}} = 13.84$ atoms/nm^2. In contrast, for Tl one finds $\rho_{\text{Tl}} = 9.66$ atoms/nm^2, i.e., the atom densities differ by ≈30 %. We determined the deposition rate by assuming that the $(\sqrt{3}\times\sqrt{3})$-reconstructed surface alloy of Tl/Ag(111) emerging in the LEED image presented in Fig. 2(b) consists of 1/3 Tl and 2/3 Ag. In fact, all coverages given below refer to a single pseudomorphic AL on the Ag(111) lattice. Therefore, if a film would consist of hcp-ordered Tl(0001) with its lower atom density, the nominal coverage needed to be corrected by a factor of 1.3 to account for the misfit. In other words, a film labeled as 1 (pseudomorphic) AL in our paper would actually appear as 1.3 AL of Tl(0001).

III. THEORETICAL METHODS

We employ DFT with the local-density approximation [46] to obtain the structural and electronic properties of the system. These calculations [47] are performed employing nonlocal norm-conserving pseudopotentials in the separable Kleinman-Bylander form [48] including scalar-relativistic corrections and spin-orbit coupling [49]. Electronic wave functions are represented by Gaussian orbitals with s, p, and d symmetries [50].

The Tl/Ag(111) $(\sqrt{3}\times\sqrt{3})$ surface alloy is described within the supercell approach. We use a slab of 17 Ag layers with $TlAg_2$ layers at top and bottom. A vacuum of 1.2 nm is employed to decouple neighboring slabs. In structure optimizations, the outmost four layers are allowed to relax. Brillouin zone integrations are carried out using a $8\times8\times1$ Monkhorst-Pack mesh [51] for the slab calculations. We obtain a silver bulk lattice constant of $a = 404$ pm which is

slightly smaller than the experimental value of $a = 409$ pm. In our structure optimization for Tl/Ag(111), we find an outward relaxation $\Delta z = 54$ pm between the Tl atom and the plane of the surface layer. This corresponds to a distance of 291 pm between Tl and Ag atoms.

The moiré structure is treated by a supercell with a large lateral unit cell. To take the mismatch between the Ag and the Tl lattice into account, we employ a (4×4) Tl layer on top of a (5×5) reconstructed Ag substrate. Using the experimental lattice constant of 348 pm for the Tl adlayer, neighboring Ag atoms have on average a distance of 278 pm in each layer. This is slightly smaller than the nearest-neighbor distance of 289 pm in bulk silver. The supercell contains a Tl layer, five Ag layers, and a hydrogen layer terminating the lower surface to inhibit the interaction between top and bottom surface states [52]. Relaxations on the topmost four layers were taken into account. The resulting nearest-neighbor distances between Tl and Ag atoms are between 294 and 326 pm.

We simulate the IPE process by assuming a plane wave as the initial state and compute the dipole transition matrix elements employing the final states resulting from our DFT calculations. An exponential damping term with a decay length of 125 pm has been used to consider the finite penetration depth of the incoming electrons.

IV. RESULTS AND DISCUSSION

A. Growth mode and atomic film structure

1. Element-specific analysis by AES

For an initial evaluation of the growth mode of Tl on Ag(111), we performed AES measurements at a primary electron energy of $E_p = 3$ keV. Figure 1 summarizes AES data measured at room temperature for samples with Tl coverages between 0.33 and 4 AL. The spectrum of clean Ag(111) (black) is given as a reference. All spectra are normalized to 1 at 100 eV. Vertical lines mark characteristic energies of AES transitions for Ag at $E^{Ag}_{AES,1} = 37$ eV and $E^{Ag}_{AES,2} = 49$ eV and for Tl at $E^{Tl}_{AES,3} = 86$ eV, in good agreement with reference data [53]. Already at a coverage of 0.33 AL (red), the Ag AES peaks are significantly attenuated and a pronounced Tl signal can be recognized. When the Tl coverage is further increased, the Ag peaks are more and more reduced, whereas no substantial increase of the Tl signal is observed at Tl coverages beyond 0.67 AL.

While this result indicates that Tl films grow reasonably flat on Ag(111)—an assessment which will later be confirmed by STM data—the saturation of the Tl signal at coverages that low is rather surprising. It is generally assumed that the escape depth of Auger electrons in the energy range between 30 and 100 eV amounts to one to two atomic layers only and is largely independent of the particular element [54–56]. Therefore, the formation and growth of second Tl layer islands on a wetting layer or a Tl-saturated surface alloy should lead to a substantial increase of the Tl-specific AES signal and to a corresponding reduction of the Ag lines. Only the latter is experimentally observed. We can only speculate about the physical origin of this behavior. A potential source may be a thickness-dependent electronic structure of Tl/Ag(111) which lowers the efficiency of the Auger process and accidentally compensates the expected increase of the AES signal.

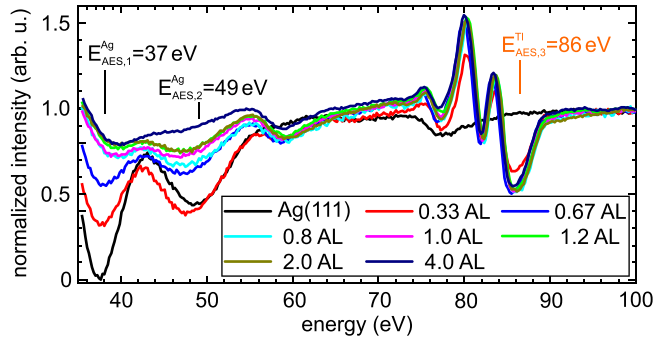

FIG. 1. Auger electron spectroscopy (AES) data of Tl/Ag(111) for Tl coverages of up to 4 AL. During Tl growth the substrate was held at a temperature $T_{sample} = 478$ K. The AES measurements were performed at room temperature at a primary electron beam energy $E_p = 3$ keV.

2. Long-range structural order by LEED

For a better understanding of the film growth and surface structures formed during Tl growth on Ag(111), we performed LEED measurements at room temperature at a primary electron energy $E^{LEED}_{kin} = 60$ eV. The results—which are displayed in Fig. 2 with inverted contrast for better visibility—were obtained on exactly the same sample preparations already presented in Fig. 1. Panel (a) shows LEED patterns of the clean Ag(111) substrate as a reference, with the hexagonal reciprocal lattice marked by blue dashed lines. The LEED patterns show first-order intensity maxima along $\overline{\Gamma M}$ directions, which correspond to the $\langle 11\bar{2}\rangle$ directions in real space. Evaluation of these spots results in a lattice constant $a_{Ag(111)} = (290 \pm 23)$ pm, in good agreement with the literature value of $a^{lit}_{Ag(111)} = 289$ pm [44].

At a coverage of 0.33 AL [see Fig. 2(b)], a new structure evolves which is marked with orange dashed lines. Analysis of the spot spacing results in a lattice constant $a = (495 \pm 26)\,\text{pm} \approx \sqrt{3}\, a^{lit}_{Ag(111)}$. Since similar superstructures were observed for $BiAg_2$ and $PbAg_2$ surface alloys on Ag(111) at the same coverage, it is reasonable to assume that this diffraction pattern indicates the presence of a $(\sqrt{3}\times\sqrt{3})$ surface reconstruction formed by $TlAg_2$. This assumption will later be supported by IPE spectra and DFT calculations. The $(\sqrt{3}\times\sqrt{3})$ spots themselves are blurred out compared to the Ag(111) ones. This is an indication that the surface alloy does not show a long-range order, most likely due to disorder and/or defects. This will be confirmed below by STM measurements.

At a coverage of 0.5 AL [see Fig. 2(c)], another structure arises around the Ag(111) spots, marked with green dashed lines. These so-called satellites show the smallest reciprocal lattice, which means they correspond to the largest real-space structure. As will be presented later, these satellite spots mark the appearance of a moiré superstructure, caused by the Tl-Ag lattice mismatch of about 16.5%. Analysis of the experimental data results in $a^{LEED}_{moiré} = (1.93 \pm 0.74)$ nm, i.e., slightly above

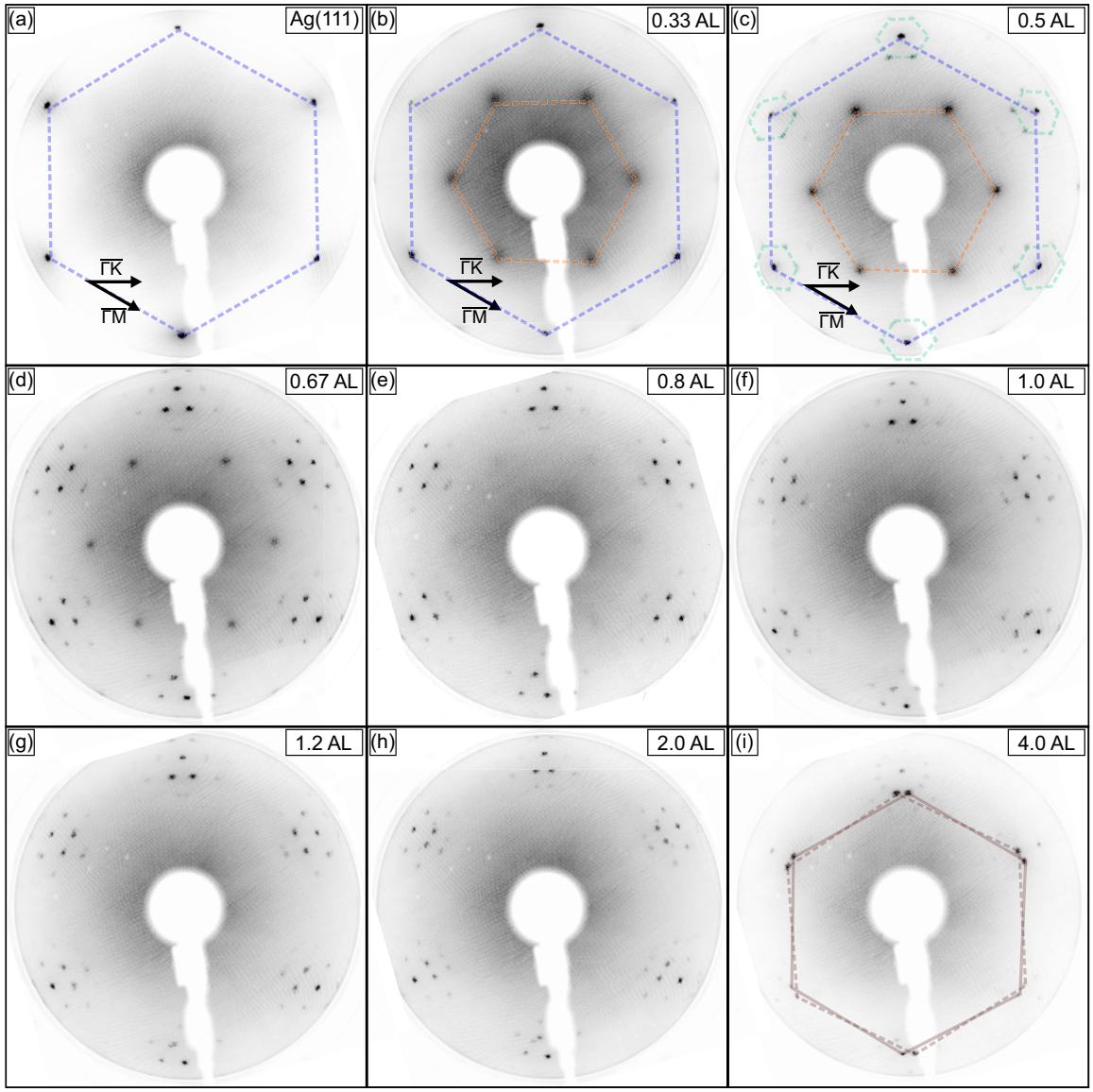

FIG. 2. Thickness-dependent LEED study for Tl/Ag(111): (a) clean Ag(111) substrate and (b)–(i) Tl film thicknesses between 0.33 and 4.0 AL. Colored hexagons indicate the hexagonal reciprocal lattice of Ag(111) (blue), the $(\sqrt{3}\times\sqrt{3})$ surface alloy (orange), the moiré superstructure (green), and the rotated reciprocal lattice of a thick Tl(111) film (brown). The LEED data were acquired at room temperature at a primary electron energy $E_{\mathrm{kin}}^{\mathrm{LEED}} = 60\,\mathrm{eV}$. During Tl growth the temperature of the Ag(111) substrate was $T_{\mathrm{sample}} = 478\,\mathrm{K}$.

the theoretically expected value of $a_{\mathrm{moiré}}^{\mathrm{lit}} = 1.78$ nm [57], as obtained on the basis of Eq. (3) in Ref. [57] with the theoretical lattice constants of Tl and Ag.

When further increasing the Tl coverage, the intensity of the $(\sqrt{3}\times\sqrt{3})$ maxima successively decreases [see Figs. 2(d) and 2(e)], until it completely vanishes at a Tl coverage of 1.0 AL [see Fig. 2(f)]. Also the intensity of the Ag(111) diffraction spots reduces, but they remain visible up to the highest coverage of 4-AL Tl studied here. As we will evidence in more detail below, this modification of the LEED pattern is caused by the formation of a closed but buckled Tl layer which replaces the $TlAg_2$ alloy phase with increasing Tl concentration. This transition is accompanied by a sharpening of the moiré pattern, indicating an improved long-range order [see Figs. 2(d)–2(h)].

Finally, when doubling the Tl coverage from Figs. 2(h)–2(i), the diffraction spots characteristic for the Ag substrate and those of the moiré structure become extremely faint. This observation is consistent with the formation of a closed and continuous Tl film. We would like to note that the Tl lattice is rotated by $\alpha_{\mathrm{LEED}} = \pm(2.50 \pm 0.20)^\circ$ with respect to the Ag(111) surface, as illustrated by brown hexagons (dashed and solid). The evaluation of the refraction spots in Fig. 2(h) results in a lattice constant for the Tl layer of $a_{\mathrm{Tl}} = (337 \pm 19)$ pm and is comparable to the expected literature value $a_{\mathrm{Tl}}^{\mathrm{lit}} = 343$ pm [45]. These findings of the LEED experiments are consistent with an earlier presented LEED, reflection high-energy electron diffraction, and AES study by Rawlings *et al.* [58] as well as x-ray scattering data by Toney *et al.* [59–61].

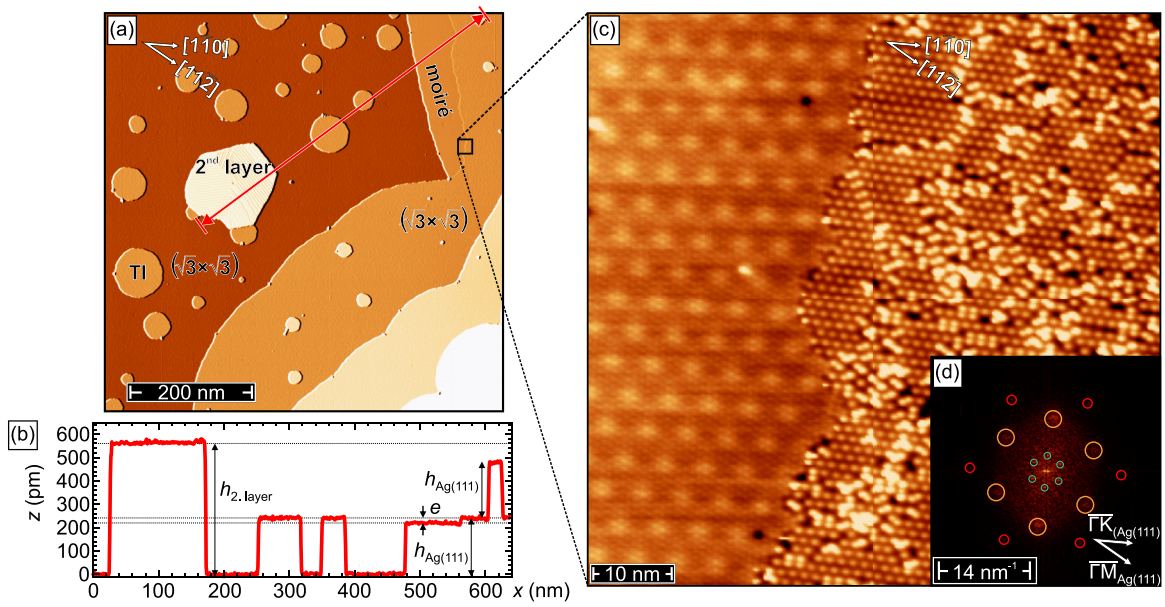

FIG. 3. STM data of a Tl film on Ag(111) with a coverage slightly above 0.33 AL. (a) STM topography overview showing overgrown step edges as well as islands with diameters between several tens of nanometers up to about 200 nm. (b) Height profile measured along the red line in panel (a). (c) Zoom-in from panel (a) showing the phase boundary between the moiré and the $(\sqrt{3}\times\sqrt{3})$ structure. (d) 2D-FFT from panel (c): cyan, moiré; orange, $(\sqrt{3}\times\sqrt{3})$; red, Tl. Scan parameters: (a) $U_{bias} = 1.0$ V, $I_{set} = 100$ pA and (c) $U_{bias} = 10$ mV, $I_{set} = 25$ nA.

3. Atomic structure by STM

a. Low Tl coverage. To better understand the atomic structure of the films, we performed STM measurements at selected Tl coverages. A low-temperature STM study ($T_{STM} \approx 4.9$ K) of a film with a Tl coverage of 0.33 AL is summarized in Fig. 3. Panel (a) shows a constant-current STM image with a scan range of 800×800 nm^2. The overall appearance of the film is governed by five atomically flat terraces. On broad terraces (width >100 nm) mostly round-shaped islands can be found. A line profile measured along the red line drawn in Fig. 3(a) is shown in Fig. 3(b). It reveals that two classes of islands can be distinguished: smaller islands with a diameter of about 20–100 nm and a height of (240 ± 5) pm and one larger island with a diameter of about 150 nm and a height of (521 ± 15) pm. The edges of the latter are roughly oriented along the $\langle 1\bar{1}0\rangle$ directions of the substrate. Furthermore, stripes vaguely along $\langle 11\bar{2}\rangle$ directions can be recognized on this higher island. Detailed inspection of the line section of Fig. 3(b) reveals an about 80-nm-wide stripe along the step edge which exhibits a slightly reduced height. While the full height difference between the two terraces amounts to the same (240 ± 5) pm already observed for the round islands, the step edge appears to be relaxed by $e = (21 \pm 1)$ pm. The first value nicely agrees with the step height expected for Ag(111), $h^{lit}_{Ag(111)} = 236$ pm, indicating that these areas are covered by the same surface structure. In contrast, the height difference between the lower terrace and the relaxed region close to the step edge is inconsistent with $h_{Ag(111)}$, most likely due to a different surface chemistry or structure.

To shed light on the origin of the relaxation we zoomed into the region indicated by a box in Fig. 3(a). The STM image of this area is displayed in Fig. 3(c). Two surface structures can clearly be distinguished. In the left part of Fig. 3(c) we recognize two coexisting periodicities, a long-period hexagonal lattice of protrusions with nearest neighbors aligned along $\langle 11\bar{2}\rangle$ directions and a separation of (1.70 ± 0.10) nm and a short-period structure along the substrate's $\langle 1\bar{1}0\rangle$ direction with a nearest-neighbor spacing of (326 ± 18) pm. The first value is consistent with the above-mentioned moiré superstructure expected for a Tl overlayer on a Ag(111) substrate of $a^{lit}_{moiré} = 1.78$ nm [57]. The second value is roughly consistent with the Tl lattice constant of 343 pm within the basal (0001) plane. In contrast to the left side, the right side of Fig. 3(c) shows only one periodicity which is roughly oriented along the $\langle 11\bar{2}\rangle$ direction. Its periodicity amounts to (508 ± 10) pm, in good agreement with a $(\sqrt{3}\times\sqrt{3})$-ordered surface alloy. It is also striking that the structure does not exhibit long-range order, but is frequently interrupted by bright spots. A more detailed discussion is presented in Ref. [41].

Figure 3(d) illustrates the corresponding two-dimensional fast Fourier transform (2D-FFT) of Fig. 3(c). We can recognize three sets of hexagonally arranged spots which are highlighted by green, orange, and red circles. The outermost (red) FFT maxima are oriented along the $\overline{\Gamma M}_{Ag(111)}$ axes and correspond to the Tl lattice which exhibits the smallest lattice constant of all surface structures. The orange spots represent the potential $(\sqrt{3}\times\sqrt{3})$-ordered $TlAg_2$ surface alloy which is rotated by $(25 \pm 1)^\circ$ with respect to the Tl lattice. The innermost (green) spots are caused by the moiré superstructure. Comparison of the FFT of the STM topography presented in Fig. 3(d) measured at $T_{STM} \approx 5$ K and the comparable LEED pattern of Fig. 2(h) taken at $T_{LEED} \approx 300$ K reveals a good agreement, thereby excluding that structural or electronic phase transitions take place in this temperature range.

b. High Tl coverage. We also performed measurements with the VT-STM on a 4-AL-thick Tl film at $T_{STM} \approx 102$ K.

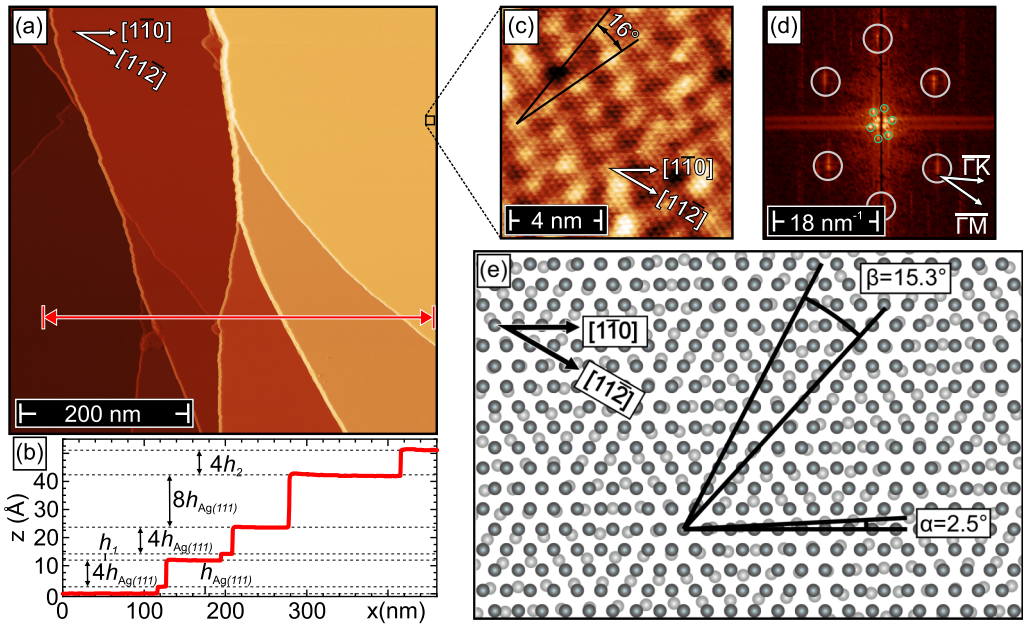

FIG. 4. (a) STM topographic overview of a 4-AL-thick Tl film grown on Ag(111) at a substrate temperature $T_{\text{sample}} = 478$ K. (b) The height profile measured along the red line in panel (a) reveals that several step edges exhibit a height which is equivalent to several atomic layers of Ag(111), with $h_{\text{Ag(111)}} = (233 \pm 4)$ pm, with two exceptions marked $h_1 = 224$ pm and $h_2 = 240$ pm. (c) High spatial resolution STM data of the same film showing two coexisting patterns with periodicities of $a_{\text{Tl}} = (348 \pm 17)$ pm and $a_{\text{moiré}} = (1.67 \pm 0.17)$ nm, corresponding to the atomic lattice of the Tl surface and the moiré superstructure, respectively. (d) 2D-FFT of the data presented in panel (c). Bragg peaks originating from the Tl atomic lattice are marked by white circles. The spots of the moiré pattern are marked with green circles. (e) Structural model of a Tl layer (dark gray) on the Ag(111) substrate (bright gray) with a rotational angle of $\alpha = \pm 2.50°$. Scan parameters: (a), (c) $U_{\text{bias}} = 200$ mV, $I_{\text{set}} = 100$ pA.

Figure 4(a) displays an overview scan showing the overall surface morphology. Eight atomically flat terraces with terrace widths between 30 and 250 nm can be recognized. The step edges separating these terraces are not straight but somewhat curved. Occasionally, the merging of two step edges into one higher step edge occurs, or vice versa. In contrast to the results presented in Fig. 3(a) for a much lower film thickness, no island growth but a closed Tl layer is observed. Similar appearances of steps and terraces can also be found on pristine Ag(111) surfaces. They are often caused by material clusters which act as pinning centers for step edges, thereby leading to the local bunching of step edges.

Figure 4(b) shows the height profile measured along the red line in panel (a). It is evident that the height of the individual step edges differs strongly. The height of those step edges marked $h_{\text{Ag(111)}}$ in Fig. 4(b) amounts to multiples of the step height of Ag(111), i.e., $h^{\text{Lit}}_{\text{Ag(111)}} = 236$ pm. Our data give $h_{\text{Ag(111)}} = (233 \pm 4)$ pm. However, two exceptions of step heights which are inconsistent with $h_{\text{Ag(111)}}$ are observed, i.e., $h_1 = 224$ pm and $h_2 = 240$ pm.

The frequent appearance of step heights which are multiples of the substrate's lattice parameter and the smoothness of the terraces indicate a homogeneous film thickness and a Tl layer which essentially follows the terrace-and-step structure of the underlying Ag(111) surface. If an inhomogeneous film with different local coverages, say n_{Tl} and $(n+1)_{\text{Tl}}$ atomic layers, would cover an atomically flat area of the substrate, the step height is expected to be equivalent to the film's lattice parameter [62]. In a similar setting, if the film thickness n_{Tl} and $(n+1)_{\text{Tl}}$ would just compensate a step edge of the underlying substrate, n_{Ag} and $(n-1)_{\text{Ag}}$, weak stripes caused by the different layer thickness of the film and the substrate shall be visible on the surface [62,63]. Both scenarios are not observed for the majority of step edges in Fig. 4. Only the step edges with height h_1 and h_2 are inconsistent with multiples of both $h^{\text{Lit}}_{\text{Ag(111)}}$ and half the Tl lattice parameter along the c axis, $h^{\text{Lit}}_{\text{Tl(0001)}} = 276$ pm. We speculate that interfacial reconstruction or stress resulting from the growth process may play a role.

The atomically resolved image presented in Fig. 4(c) and its 2D-FFT in Fig. 4(d) allow for a detailed analysis of the two hexagonal lattice periodicities visible in real and reciprocal space, respectively. For the shorter real space lattice, the $\langle 1\bar{1}0 \rangle$ nearest neighbors have a spacing of $a = (348 \pm 17)$ pm. In comparison with earlier observations in Refs. [58,64], this can be interpreted as a pure Tl layer. The larger pattern has a periodicity of $a^{\text{STM}}_{\text{moiré}} = (1.67 \pm 0.17)$ nm and is identified with the moiré pattern formed between the Ag substrate and the Tl overlayer. This value is in good agreement with the results of the LEED measurements presented in Fig. 2. Close inspection reveals that the Tl layer is rotated by an angle $\beta = (16 \pm 2)°$ with respect to the moiré lattice. Using the formalism developed by Wiederholt *et al.* [65], knowledge of the angle β allows for the calculation of the rotation α of this Tl layer with respect to the Ag(111) substrate. From the structural model of the rotated Tl layer (dark gray) with respect to the Ag(111) substrate (bright gray) presented in Fig. 4(e), the rotation β between the moiré superstructure and

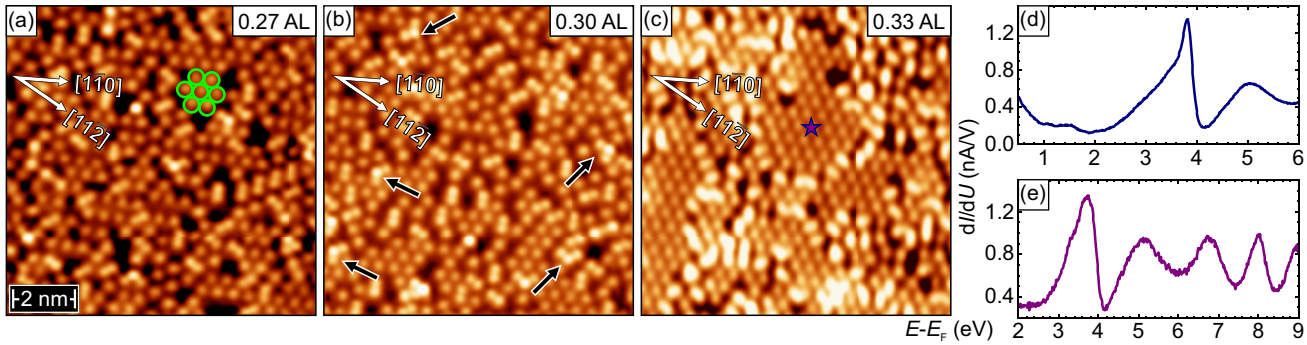

FIG. 5. Coverage-dependent series of STM images of Tl on Ag(111): (a) 0.27 AL, (b) 0.30 AL, and (c) 0.33 AL. The size of $(\sqrt{3}\times\sqrt{3})$-ordered domains increases from panel (a) to panel (c). Scan parameters: $U_{\text{bias}} = 10\,\text{mV}$, $I_{\text{set}} = 100\,\text{pA}$. (d), (e) dI/dU spectra taken with an active feedback loop at the position marked with a purple star in panel (c). STS parameters: (d) $U_{\text{mod}} = 10\,\text{mV}$, $I_{\text{set}} = 1\,\text{nA}$, $\nu = 733\,\text{Hz}$ and (e) $U_{\text{mod}} = 30\,\text{mV}$, $I_{\text{set}} = 250\,\text{pA}$, $\nu = 733\,\text{Hz}$.

the Tl layer can be graphically determined. Our assessment results in $\beta = 15.3^\circ$ [also marked in Fig. 4(e)] and $\alpha_{\text{theo}} = \pm 2.50^\circ$. With $a^{\text{lit}}_{\text{Ag(111)}} = 289\,\text{pm}$ [44], the experimentally determined values for $\beta = (16.3 \pm 1.6)^\circ$ [see Fig. 4(c)] and $a^{\text{STM}}_{\text{Tl}} = (348 \pm 17)\,\text{pm}$, it follows that $\alpha_{\text{Tl}} = (2.81 \pm 0.71)^\circ$. This value is thus consistent with the rotation of $\alpha_{\text{LEED}} = \pm(2.50 \pm 0.20)^\circ$ measured by LEED in Fig. 2(i), but somewhat below the 3°–5° previously observed experimentally by Rawlings *et al.* [58], Carnal *et al.* [64], and Toney *et al* [61].

B. Electronic structure

In the following section, we will present and discuss the electronic properties of the $(\sqrt{3}\times\sqrt{3})$-ordered $TlAg_2$ surface alloy and the moiré superstructure of Tl/Ag(111) as determined by means of STS and IPE spectra as well as DFT calculations.

1. *The* $(\sqrt{3}\times\sqrt{3})$ $TlAg_2$ *surface alloy*

Figures 5(a)–5(c) summarize the evolution of the $(\sqrt{3}\times\sqrt{3})$ surface alloy with increasing Tl deposition in a narrow coverage range just below 0.33 AL as observed with STM. For a coverage of 0.27 AL [see Fig. 5(a)], only tiny patches with a C_6 rotational invariance appear. Inspection of some examples, indicated by green colored circles, shows nearest-neighbor protrusions aligned along $\langle 11\bar{2}\rangle$ directions which are separated by $(492 \pm 10)\,\text{pm}$. These values are in agreement with the data expected for the $(\sqrt{3}\times\sqrt{3})$ reconstruction for the stoichiometry $TlAg_2$. This indicates that the surface structure shown in Fig. 5(a) represents a situation where this surface alloy has begun to form but is not yet fully established. Regions with a smaller or larger separation between adjacent maxima appear dark or bright, respectively.

For an increased coverage of 0.30 AL [see Fig. 5(b)], the $(\sqrt{3}\times\sqrt{3})$-ordered regions of the $TlAg_2$ surface alloy occupy a significantly larger share of the surface area. The typical size of ordered domains amounts to 1 to 2 nm. Occasionally, bright dimers or chevrons (see arrows) can be found, probably representing Tl atoms with a lower nearest-neighbor distance of $(340 \pm 10)\,\text{pm}$, i.e., much shorter than the $\sqrt{3}\,a^{\text{lit}}_{\text{Ag(111)}}$ expected for the $(\sqrt{3}\times\sqrt{3})$ reconstruction. Finally, at a coverage of 0.33 AL shown in Fig. 5(c) we see that the surface is almost completely covered by $(\sqrt{3}\times\sqrt{3})$-ordered domains with a typical size of about 5 nm. Structural domain boundaries can be recognized by bright or dark regions with an enhanced or reduced Tl density, respectively.

The purple star in Fig. 5(c) marks the position where the point dI/dU spectra presented in Figs. 5(d) and 5(e) were taken. Both spectra were recorded under closed feedback loop conditions to avoid an overload of the lock-in amplifier. To map the unoccupied electronic states between just above the Fermi level and about the vacuum level we initially restricted the energy range to $0.5 \leqslant E - E_{\text{F}} \leqslant 6.0\,\text{eV}$ [see Fig. 5(d)]. Following the spectrum from low to high energy, we recognize a rather weak feature at $E - E_{\text{F}} \approx 1.5\,\text{eV}$. At around $E - E_{\text{F}} \approx 2.2\,\text{eV}$, a broad, almost linear slope arises which reaches up to about $E - E_{\text{F}} \approx 3.6\,\text{eV}$, where the slope becomes steeper until it peaks in a sharp maximum at $E - E_{\text{F}} = 3.8\,\text{eV}$. To follow the dI/dU signal over a wider energy range reaching far above the vacuum level, we took another spectrum in the range $2 \leqslant E - E_{\text{F}} \leqslant 9\,\text{eV}$ [see Fig. 5(e)]. In both spectra, i.e., Figs. 5(d) and 5(e), we see a deep dip just above $E - E_{\text{F}} \approx 4\,\text{eV}$ followed by a broad peak at $E - E_{\text{F}} \approx 5\,\text{eV}$. At even higher energies three further oscillations of the dI/dU signal with peaks at about 6.7, 8, and 9 eV can be recognized.

The angular dispersion of unoccupied states within the energy region covered by STS has been measured with IPE. For the IPE spectra of the $(\sqrt{3}\times\sqrt{3})$ surface alloy, a deposition of slightly more than 0.33 AL was chosen to be sure that the best possible $(\sqrt{3}\times\sqrt{3})$ surface alloy is formed. From the STM data in Fig. 3(c) it is obvious that even at this coverage the structural order of the surface alloy is far from being perfect and in LEED the moiré superstructure starts to appear. The IPE spectra for the $\overline{\Gamma\text{K}}$ direction of the surface alloy [corresponding to $\overline{\Gamma\text{M}}$ of the Ag(111) substrate] are displayed in Fig. 6. As seen in Fig. 6(a), a spectral feature with low intensity is visible at 1.7 eV for normal electron incidence. This peak disperses downward in energy with increasing angle θ, highlighted by the green line, while losing intensity. At energies higher than 2.5 eV, an intensity increase indicates the appearance of another spectral feature. In Fig. 6(b) IPE spectra for extended energy and angle ranges are presented. A prominent feature at 3.2 eV highlighted by a blue line exhibits a weak positive energy dispersion with increasing θ.

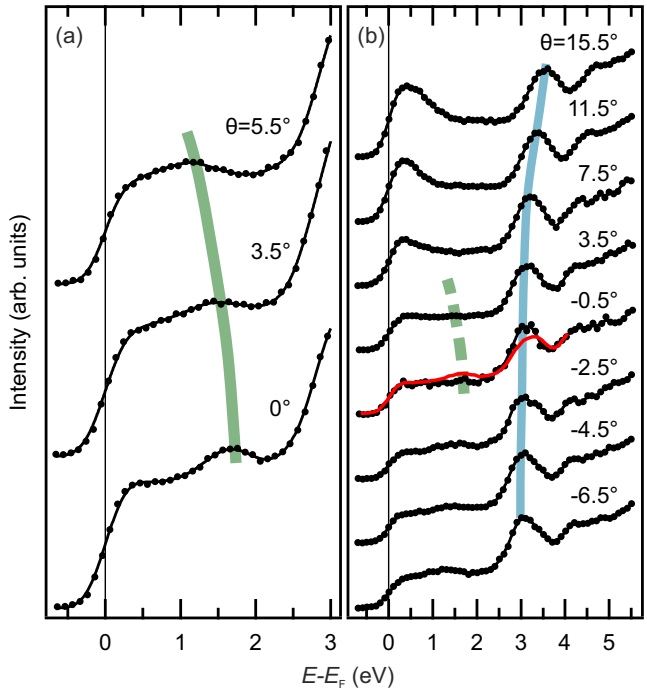

FIG. 6. (a) IPE spectra of the $(\sqrt{3}\times\sqrt{3})$ surface alloy for three angles of electron incidence θ along $\overline{\Gamma K}$. For normal electron incidence, a spectral feature appears at 1.7 eV which disperses downward in energy with increasing θ. (b) IPE spectra for a larger energy and angle range. At around 3 eV, a prominent feature is visible highlighted by the blue line. The red line in panel (b) represents the 0° spectrum of panel (a) overlayed on the -0.5° spectrum.

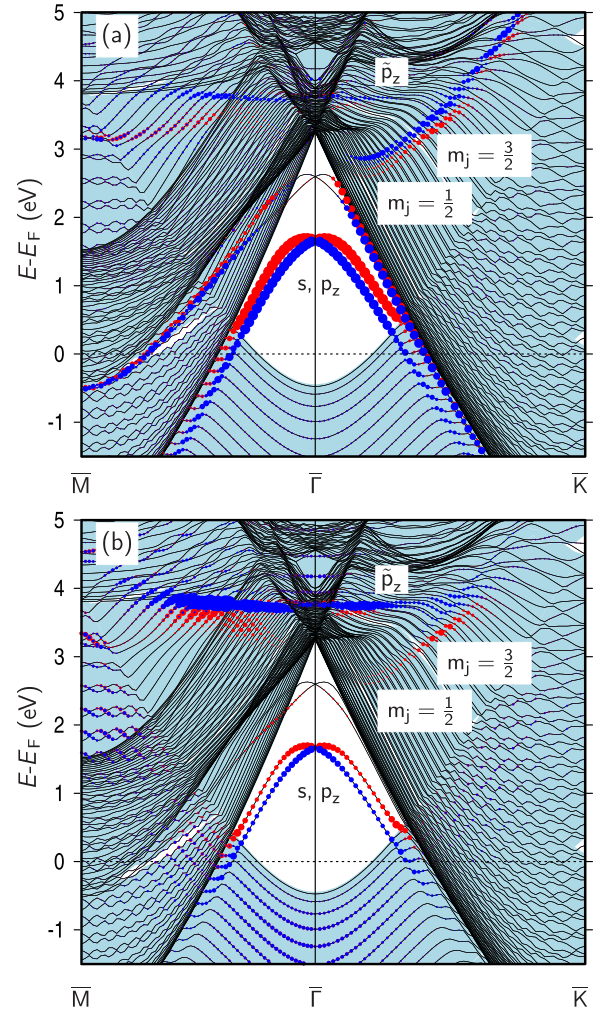

FIG. 7. Band structure of the $(\sqrt{3}\times\sqrt{3})$ surface alloy along $\overline{\Gamma M}$ and $\overline{\Gamma K}$. The surface-projected bulk band structure is indicated by the light blue shaded area. (a) Red (blue) dots indicate the Rashba component of the spin expectation value for spin-up (spin-down) electrons of surface states. (b) Calculations including matrix elements with free-electron-like initial states to model IPE results with $\hbar\omega = 9.9$ eV. The dot size is a measure of the expected spectral intensity.

There is an obvious difference between the spectra in Figs. 6(a) and 6(b) although there is no difference in the respective LEED patterns: The spectral feature at 1.7 eV clearly visible in Fig. 6(a) is reduced in Fig. 6(b) while the feature at 3.2 eV is enhanced and shifted to lower energies. For direct comparison, the 0° spectrum of Fig. 6(a) is overlayed on the -0.5° spectrum in panel (b). This again underlines that the preparation of the $(\sqrt{3}\times\sqrt{3})$ structure is delicate.

A comparison with the dI/dU spectra of Fig. 5(d) shows rather good agreement for the state around 1.6 eV but less agreement for the states above 3 eV. The blue highlighted IPE feature may be included in the broad STS feature above 3 eV but the sharp STS feature at 3.8 eV has no equivalent in the IPE spectra. In this context we want to emphasize that the STS results shown in Fig. 5 originate from the center of a perfectly ordered $(\sqrt{3}\times\sqrt{3})$ patch while IPE integrates over a large surface area in the mm range, averaging over ordered and less ordered areas.

For higher energies, an additional steplike feature (with a small peak in some spectra) is visible in the IPE spectra at $\approx$4.2 eV that disperses to higher energies for positive and negative angles. Given the measured work function of (4.43 ± 0.03) eV, this step and small peak are attributed to an image-potential state/resonance [66,67]. The first image-potential resonance in the STS experiment appears at $\approx$5 eV, approximately 1 eV higher than in IPE. The difference can be explained by the changed surface potential due to the applied voltage in the STS experiment [68,69].

To interpret the STS and IPE results and their differences, we have calculated the electronic band structure of the $(\sqrt{3}\times\sqrt{3})$ system via DFT. The results are displayed in Fig. 7. The blue-shaded areas mark the surface-projected bulk band structure. In Fig. 7(a) the red (blue) dots indicate the Rashba component of the spin expectation value for spin-up (spin-down) electrons of surface states. The s, p_z-derived surface band is typical for XAg_2 surface alloys with X being a heavy transition metal. This state appears at $\overline{\Gamma}$ at 1.7 eV and is observed both in STS and IPE, yet as a rather broad feature with small intensity. Also, this state shows a downward energy dispersion, as observed in the IPE experiment. This dispersion may explain the slightly lower energy of 1.5 eV in the STS spectrum. The calculation predicts a Rashba-type spin splitting with a Rashba energy $E_R \approx 25$ meV. Due to the low spectral intensity and broad linewidth, this splitting could not be confirmed via spin-resolved IPE (spectra not shown).

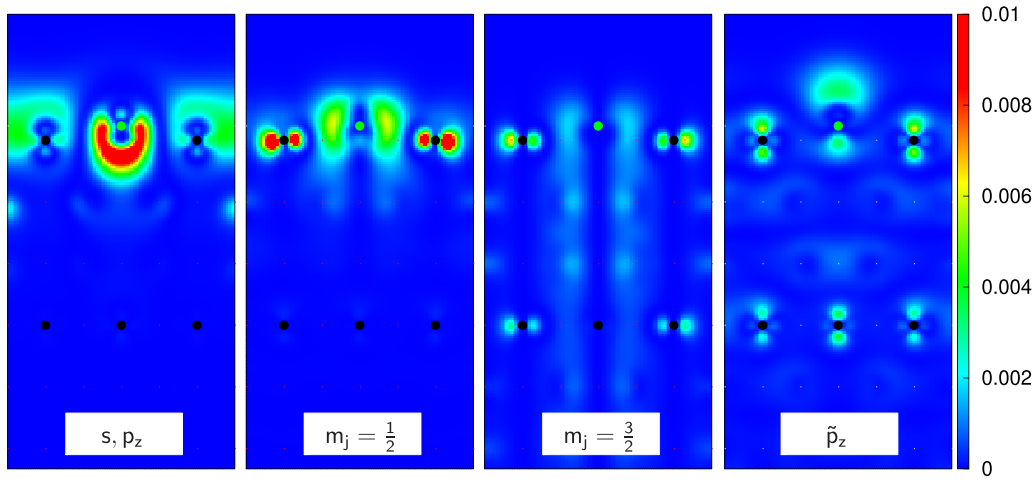

FIG. 8. Charge-distribution plots of surface states at $\overline{\Gamma}$ for the $(\sqrt{3}\times\sqrt{3})$ surface alloy. The green (black) circles indicate the positions of the Tl (Ag) atoms in the drawing plane. The charge density is given in units of $a_B^{-1/3}$. The states $m_j = 3/2$ and $\tilde{p}_z$ are energetically resonant with silver bulk states.

The $m_j = 1/2$ state is predicted to lie at higher energies within the surface-projected band gap, while the $m_j = 3/2$ state overlaps with bulk states. These states were not found in IPE experiments. To get more insight, we have modeled the IPE results by including transitions matrix elements from free-electron-like initial states. The results of this calculation are displayed in Fig. 7(b) with the dot size being a measure of the IPE intensity. Here, the s, p_z band is expected to exhibit a pronounced intensity in IPE, contrary to the $m_j = 1/2$ and $3/2$ states. The latter states may be responsible for the already mentioned STS intensity between 2.2 and 3.6 eV. An additional band with p_z symmetry, labeled $\tilde{p}_z$, appears at 3.7 eV in the calculation with almost no energy dispersion. The energy of this state fits nicely to the strong STS intensity at 3.8 eV while the IPE feature at 3.2 eV resembles the energy dispersion but deviates in energy.

Noticeably, the $\tilde{p}_z$ state has a much higher intensity than the s, p_z state, especially in the STS measurements even though both have p_z character. A possible explanation can be found in the charge distribution of the four different surface states plotted in Fig. 8. The charge distribution of the s, p_z state reveals that this state is mainly located around the Tl atoms, with the main distribution between the surface and the second atomic layer. It appears that this state has almost no extension into the vacuum which explains the very low intensity in the STS experiment. The $m_j = 1/2$ and $3/2$ state have a p_x, p_y character, with the most charge located at the Ag atoms. In comparison with the s, p_z state, the $\tilde{p}_z$ state is not located mainly at the Tl atoms, but has a similar charge distribution at all surface atoms and a nonvanishing charge distribution in the fourth layer. Additionally, the charge distribution in front of the surface is much higher, resulting in a strong intensity in the STS measurement.

2. *The moiré superstructure*

For the moiré superstructure similar data sets as for the $(\sqrt{3}\times\sqrt{3})$ surface alloy were measured. The topographic STM image presented in Fig. 9(a) shows the surface atomic lattice of a Tl layer which is superimposed by the much longer modulation of the moiré superstructure. The red star marks the position where the point spectra of Figs. 9(b) and 9(c) were measured. The dI/dU point spectrum in Fig. 9(b) shows again the energy range $0.5 \leqslant E - E_F \leqslant 6.0$ eV. We see an extremely sharp maximum at $E - E_F = 3.2$ eV which is followed by a small hump at $E - E_F \approx 3.4$ eV, followed by oscillations that can be assigned to the image-potential resonances of thallium. The curvature of the left shoulder of the sharp maximum might indicate a holelike state. Only one image-potential surface state appears in the quite narrow energy range of Fig. 9(b); another one is detected for a wider energy range of Fig. 9(c) ($E - E_F = 2.0$–6.5 eV). For the IPE experiments of the moiré superstructure a Tl coverage of $\approx$ 0.8 AL was used. The resulting spectra for the $\overline{\Gamma M}$ direction of the Ag(111) substrate are shown in Fig. 10. The spectra in Fig. 10(a) show two parabolically dispersing features. The first feature at 3.0 eV has an effective mass of $m^*/m_e = 1.6 \pm 0.2$. It corresponds to the first peak in the STS spectra at 3.2 eV. Spin-resolved IPE spectra for three exemplary angles

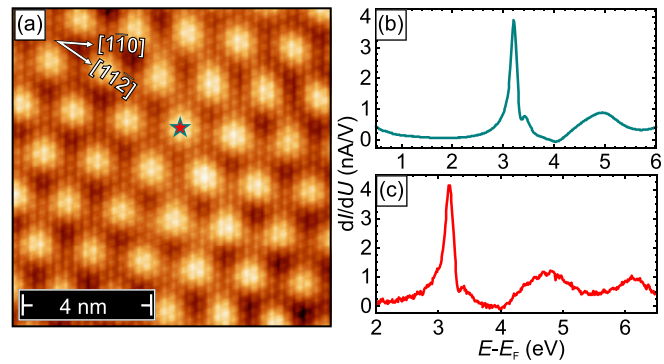

FIG. 9. (a) Atomic resolution STM topography data of the moiré superstructure. (b), (c) dI/dU spectra taken at the position marked with a red star in panel (a). Scan parameters: (a) $U_{bias} = 10$ mV, $I_{set} = 25$ nA. STS parameters: (b) $U_{mod} = 10$ mV, $I_{set} = 1$ nA, $\nu = 733$ Hz, feedback loop active and (c) $U_{mod} = 5$ mV, $\nu = 733$ Hz, feedback loop off.

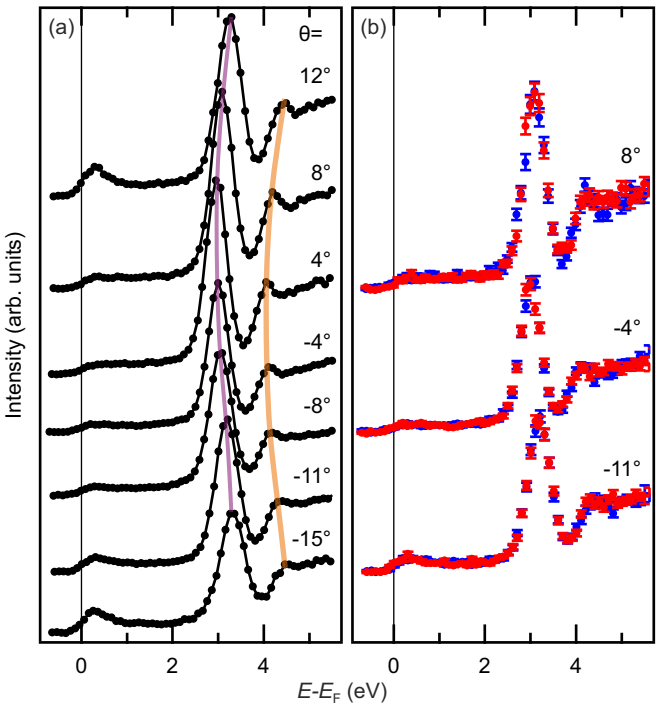

FIG. 10. (a) Spin-integrated IPE spectra for various angles of incidence showing two parabolic dispersing features. The parabolic dispersion is sketched via a guide to the eye (purple and orange lines). (b) Spin-resolved spectra for three exemplary angles.

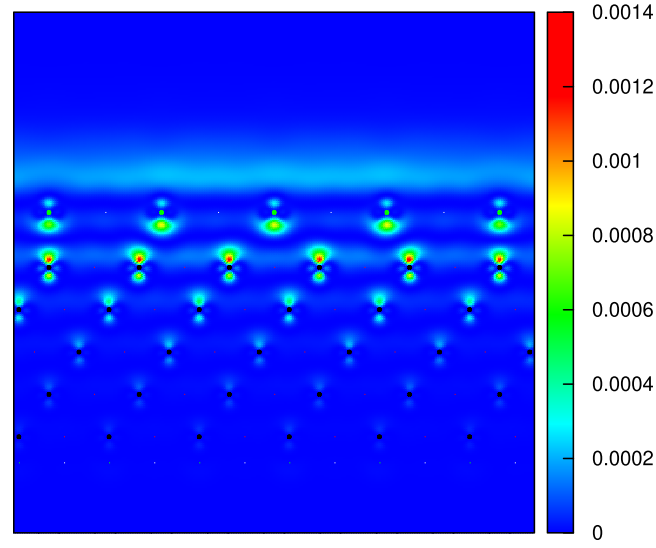

FIG. 11. Charge-distribution plot of the surface state at $\overline{\Gamma}$ for the moiré superstructure. The green (black) circles indicate the positions of the Tl (Ag) atoms in the drawing plane. The drawing plane is rotated by 90° with respect to the drawing plane used in Fig. 8. The charge density is given in units of $a_B^{-1/3}$.

displayed in Fig. 10(b) show no Rashba-type spin splitting for any state. This behavior is at first glance not expected for a surface state of a heavy material such as Tl with high atomic number Z.

The second feature at $E - E_F = 4.0\,\text{eV}$ is attributed to an image-potential state/resonance and shows an effective mass of $m^*/m_e = 1.2 \pm 0.1$. With the work function of $\phi = 4.3\,\text{eV}$ the binding energy with respect to the vacuum energy results in 0.3 eV. This value is low compared with typical binding energies of 0.38 up to 0.85 eV for image states, depending on their position within the energy gap [66,67]. In the present case, the image states overlap with Tl/Ag states thereby forming image resonances.

To explain the missing Rashba splitting, we have calculated the charge distribution of the surface state appearing at about 3 eV plotted in Fig. 11. This calculation shows that the state has mainly p_z character and additionally a distinct charge density in front of the surface which results in a high STS intensity. Due to the almost pure p_z character with some admixtures of d_{z^2} the orbital angular momentum which is a measure of a Rashba-type spin splitting almost vanishes [70]. As a consequence, no spin splitting is predicted for this state around $\overline{\Gamma}$ as it is observed in the IPE experiment.

The calculations reveal a further interesting detail. The surface state for the moiré superstructure exhibits a similar charge distribution as the $\tilde{p}_z$ state on the $(\sqrt{3}\times\sqrt{3})$ surface alloy, yet modified by Ag surface atoms. Furthermore, it appears at somewhat lower energy for the moiré superstructure in experiment and theory. This detail may explain the deviation of energies in STS and IPE experiments for the $\tilde{p}_z$ state of the $(\sqrt{3}\times\sqrt{3})$ surface alloy. Since IPE averages over $(\sqrt{3}\times\sqrt{3})$ and moiré patches, the energy of $\tilde{p}_z$ appears at lower energy compared with STS. This energy shift is supported by IPE spectra for two preparations shown in Fig. 6(b).

V. CONCLUSION

We studied the structural and electronic properties of ultrathin Tl films on Ag(111). At coverages around 0.33 AL, a $(\sqrt{3}\times\sqrt{3})$ $TlAg_2$ surface alloy evolves. This structure forms small domains interrupted by multiple defects. For higher coverages a closed monolayer is formed with a moiré superstructure due to different lattice constants of Tl and Ag. In this case, the Tl layer is rotated by $\pm(2.50 \pm 0.20)^\circ$ with respect to the Ag(111) substrate. This moiré superstructure is also visible for film thicknesses up to 4 AL.

Based on STS and IPE experiments as well as DFT calculations, we identified the surface electronic structure of the $(\sqrt{3}\times\sqrt{3})$ surface alloy and the moiré superstructure. In particular, we analyzed an s, p_z-derived surface state with a theoretically predicted Rashba energy of 25 meV for the $TlAg_2$ surface alloy, a p_z-derived surface state without Rashba splitting for both $(\sqrt{3}\times\sqrt{3})$ surface alloy and moiré superstructure, and image-potential resonances. The experimental results were described and explained by comprehensive calculations for the band structure and charge distributions of the respective electronic states.

ACKNOWLEDGMENTS

S.S. and M.D. thank Th. J. Welling for his help with the sample preparation. This work was supported by the Deutsche Forschungsgemeinschaft (DFG) through SFB 1170 (Project No. C02). We also acknowledge financial support

by the DFG under Germany's Excellence Strategy through Würzburg-Dresden Cluster of Excellence on Complexity and Topology in Quantum Matter ct.qmat, through EXC 2147 (Project No. 390858490).

[1] E. I. Rashba, Properties of semiconductors with an extremum loop. I. Cyclotron and combinational resonance in a magnetic field perpendicular to the plane of the loop, Sov. Phys. Solid State **2**, 1109 (1960).

[2] Y. A. Bychkov and E. I. Rashba, Oscillatory effects and the magnetic susceptibility of carriers in inversion layers, J. Phys. C **17**, 6039 (1984).

[3] J. Nitta, T. Akazaki, H. Takayanagi, and T. Enoki, Gate Control of Spin-Orbit Interaction in an Inverted $In_{0.53}Ga_{0.47}As/In_{0.52}Al_{0.48}As$ Heterostructure, Phys. Rev. Lett. **78**, 1335 (1997).

[4] G. Dresselhaus, Spin-orbit coupling effects in zinc blende structures, Phys. Rev. **100**, 580 (1955).

[5] S. LaShell, B. A. McDougall, and E. Jensen, Spin Splitting of an Au(111) Surface State Band Observed with Angle Resolved Photoelectron Spectroscopy, Phys. Rev. Lett. **77**, 3419 (1996).

[6] G. Nicolay, F. Reinert, S. Hüfner, and P. Blaha, Spin-orbit splitting of the L-gap surface state on Au(111) and Ag(111), Phys. Rev. B **65**, 033407 (2001).

[7] F. Reinert, G. Nicolay, S. Schmidt, D. Ehm, and S. Hüfner, Direct measurements of the *L*-gap surface states on the (111) face of noble metals by photoelectron spectroscopy, Phys. Rev. B **63**, 115415 (2001).

[8] F. Reinert, Spin-orbit interaction in the photoemission spectra of noble metal surface states, J. Phys.: Condens. Matter **15**, S693 (2003).

[9] H. Cercellier, C. Didiot, Y. Fagot-Revurat, B. Kierren, L. Moreau, D. Malterre, and F. Reinert, Interplay between structural, chemical, and spectroscopic properties of Ag/Au(111) epitaxial ultrathin films: A way to tune the Rashba coupling, Phys. Rev. B **73**, 195413 (2006).

[10] S. N. P. Wissing, C. Eibl, A. Zumbülte, A. B. Schmidt, J. Braun, J. Minár, H. Ebert, and M. Donath, Rashba-type spin splitting at Au(111) beyond the Fermi level: The other part of the story, New J. Phys. **15**, 105001 (2013).

[11] The Rashba energy E_R is defined as the difference between the crossing point at $k_\parallel = 0$ and the band onsets E_0 of the Rashba-split bands.

[12] C. R. Ast, J. Henk, A. Ernst, L. Moreschini, M. C. Falub, D. Pacilé, P. Bruno, K. Kern, and M. Grioni, Giant Spin Splitting through Surface Alloying, Phys. Rev. Lett. **98**, 186807 (2007).

[13] L. Petersen and P. Hedegård, A simple tight-binding model of spin-orbit splitting of sp-derived surface states, Surf. Sci. **459**, 49 (2000).

[14] G. Bihlmayer, Y. M. Koroteev, P. M. Echenique, E. V. Chulkov, and S. Blügel, The Rashba-effect at metallic surfaces, Surf. Sci. **600**, 3888 (2006).

[15] M. Heide, G. Bihlmayer, Ph. Mavropoulos, A. Bringer, and S. Blügel, Spin orbit driven physics at surfaces, Newsletter of the Psi-K Network **78**, 2 (2006).

[16] G. Bihlmayer, S. Blügel, and E. V. Chulkov, Enhanced Rashba spin-orbit splitting in Bi/Ag(111) and Pb/Ag(111) surface alloys from first principles, Phys. Rev. B **75**, 195414 (2007).

[17] C. R. Ast, G. Wittich, P. Wahl, R. Vogelgesang, D. Pacilé, M. C. Falub, L. Moreschini, M. Papagno, M. Grioni, and K. Kern, Local detection of spin-orbit splitting by scanning tunneling spectroscopy, Phys. Rev. B **75**, 201401(R) (2007).

[18] C. R. Ast, D. Pacilé, L. Moreschini, M. C. Falub, M. Papagno, K. Kern, M. Grioni, J. Henk, A. Ernst, S. Ostanin, and P. Bruno, Spin-orbit split two-dimensional electron gas with tunable Rashba and Fermi energy, Phys. Rev. B **77**, 081407(R) (2008).

[19] F. Meier, H. Dil, J. Lobo-Checa, L. Patthey, and J. Osterwalder, Quantitative vectorial spin analysis in angle-resolved photoemission: Bi/Ag(111) and Pb/Ag(111), Phys. Rev. B **77**, 165431 (2008).

[20] I. Gierz, B. Stadtmüller, J. Vuorinen, M. Lindroos, F. Meier, J. H. Dil, K. Kern, and C. R. Ast, Structural influence on the Rashba-type spin splitting in surface alloys, Phys. Rev. B **81**, 245430 (2010).

[21] F. Meier, V. Petrov, S. Guerrero, C. Mudry, L. Patthey, J. Osterwalder, and J. H. Dil, Unconventional Fermi surface spin textures in the $Bi_xPb_{1-x}/Ag(111)$ surface alloy, Phys. Rev. B **79**, 241408(R) (2009).

[22] C. Kato, Y. Aoki, and H. Hirayama, Scanning tunneling microscopy of Bi-induced Ag(111) surface structures, Phys. Rev. B **82**, 165407 (2010).

[23] D. Guan, M. Bianchi, S. Bao, E. Perkins, F. Meier, J. H. Dil, J. Osterwalder, and P. Hofmann, Strongly enhanced electron-phonon coupling in the Rashba-split state of the Bi/Ag(111) surface alloy, Phys. Rev. B **83**, 155451 (2011).

[24] H. Hirayama, Y. Aoki, and C. Kato, Quantum Interference of Rashba-Type Spin-Split Surface State Electrons, Phys. Rev. Lett. **107**, 027204 (2011).

[25] K. H. L. Zhang, I. M. McLeod, M. Lahti, K. Pussi, and V. R. Dhanak, The evolution of the electronic structure at the Bi/Ag(111) interface studied using photoemission spectroscopy, J. Phys.: Condens. Matter **24**, 435502 (2012).

[26] L. El-Kareh, P. Sessi, T. Bathon, and M. Bode, Quantum Interference Mapping of Rashba-Split Bloch States in Bi/Ag(111), Phys. Rev. Lett. **110**, 176803 (2013).

[27] I. Gierz, F. Meier, J. H. Dil, K. Kern, and C. R. Ast, Tuning the spin texture in binary and ternary surface alloys on Ag(111), Phys. Rev. B **83**, 195122 (2011).

[28] L. Moreschini, A. Bendounan, H. Bentmann, M. Assig, K. Kern, F. Reinert, J. Henk, C. R. Ast, and M. Grioni, Influence of the substrate on the spin-orbit splitting in surface alloys on (111) noble-metal surfaces, Phys. Rev. B **80**, 035438 (2009).

[29] H. Bentmann, F. Forster, G. Bihlmayer, E. V. Chulkov, L. Moreschini, M. Grioni, and F. Reinert, Origin and manipulation of the Rashba splitting in surface alloys, Europhys. Lett. **87**, 37003 (2009).

[30] H. Mirhosseini, J. Henk, A. Ernst, S. Ostanin, C.-T. Chiang, P. Yu, A. Winkelmann, and J. Kirschner, Unconventional spin topology in surface alloys with Rashba-type spin splitting, Phys. Rev. B **79**, 245428 (2009).

[31] H. Bentmann and F. Reinert, Enhancing and reducing the Rashba-splitting at surfaces by adsorbates: Na and Xe on Bi/Cu(111), New J. Phys. **15**, 115011 (2013).

[32] L. El-Kareh, G. Bihlmayer, A. Buchter, H. Bentmann, S. Blügel, F. Reinert, and M. Bode, A combined experimental and theoretical study of Rashba-split surface states on the $(\sqrt{3}\times\sqrt{3})$ Pb/Ag(111)$R30^\circ$ surface, New J. Phys. **16**, 045017 (2014).

[33] L. Moreschini, A. Bendounan, I. Gierz, C. R. Ast, H. Mirhosseini, H. Höchst, K. Kern, J. Henk, A. Ernst, S. Ostanin, F. Reinert, and M. Grioni, Assessing the atomic contribution to the Rashba spin-orbit splitting in surface alloys: Sb/Ag(111), Phys. Rev. B **79**, 075424 (2009).

[34] F. Meier, V. Petrov, H. Mirhosseini, L. Patthey, J. Henk, J. Osterwalder, and J. H. Dil, Interference of spin states in photoemission from Sb/Ag(111) surface alloys, J. Phys.: Condens. Matter **23**, 072207 (2011).

[35] S. N. P. Wissing, A. B. Schmidt, H. Mirhosseini, J. Henk, C. R. Ast, and M. Donath, Ambiguity of Experimental Spin Information from States with Mixed Orbital Symmetries, Phys. Rev. Lett. **113**, 116402 (2014).

[36] S. D. Stolwijk, H. Wortelen, A. B. Schmidt, and M. Donath, Rotatable spin-polarized electron source for inverse-photoemission experiments, Rev. Sci. Instrum. **85**, 013306 (2014).

[37] A. Zumbülte, A. B. Schmidt, and M. Donath, Momentum resolution in inverse photoemission, Rev. Sci. Instrum. **86**, 013908 (2015).

[38] C. Thiede, I. Niehues, A. B. Schmidt, and M. Donath, The acetone bandpass detector for inverse photoemission: Operation in proportional and Geiger-Müller modes, Meas. Sci. Technol. **29**, 065901 (2018).

[39] S. Schemmelmann, P. Krüger, F. Schöttke, and M. Donath, Rashba-split surface state and spin-dependent photon emission from Re(0001) at $\overline{\Gamma}$, Phys. Rev. B **104**, 205425 (2021).

[40] M. Budke, T. Allmers, M. Donath, and G. Rangelov, Combined experimental setup for spin- and angle-resolved direct and inverse photoemission, Rev. Sci. Instrum. **78**, 113909 (2007).

[41] See Supplemental Material at http://link.aps.org/supplemental/10.1103/PhysRevB.107.205144 for detailed information on the cleanliness of the Ag(111) substrate, a temperature-dependent LEED study, a comparison of the growth behavior in Würzburg and Münster, the growth anomaly observed for continuous or consecutive deposition, and a detailed analysis of the structural domain boundaries observed around the $(\sqrt{3}\times\sqrt{3})$-ordered $TlAg_2$ alloy. The Supplemental Material also contains Refs. [42,43].

[42] G. Nicolay, F. Reinert, S. Schmidt, D. Ehm, P. Steiner, and S. Hüfner, Natural linewidth of the Ag(111) L-gap surface state as determined by photoemission spectroscopy, Phys. Rev. B **62**, 1631 (2000).

[43] S. Wilfert, M. Schmitt, H. Schmidt, T. Mauerer, P. Sessi, H. Wang, Q. Mao, M. Fang, and M. Bode, Scanning tunneling microscopy and spectroscopy studies of the heavy-electron superconductor $TlNi_2Se_2$, Phys. Rev. B **97**, 014514 (2018).

[44] W. P. Davey, Precision measurements of the lattice constants of twelve common metals, Phys. Rev. **25**, 753 (1925).

[45] H. Lipson and A. R. Stokes, Structures of Thallium, Nature (London) **148**, 437 (1941).

[46] J. P. Perdew and A. Zunger, Self-interaction correction to density-functional approximations for many-electron systems, Phys. Rev. B **23**, 5048 (1981).

[47] B. Stärk, P. Krüger, and J. Pollmann, Magnetic anisotropy of thin Co and Ni films on diamond surfaces, Phys. Rev. B **84**, 195316 (2011).

[48] L. Kleinman and D. M. Bylander, Efficacious Form for Model Pseudopotentials, Phys. Rev. Lett. **48**, 1425 (1982).

[49] L. A. Hemstreet, C. Y. Fong, and J. S. Nelson, First-principles calculations of spin-orbit splittings in solids using nonlocal separable pseudopotentials, Phys. Rev. B **47**, 4238 (1993).

[50] We use linear combinations of Gaussian orbitals [71] with different decay constants which have been determined by minimalization of the total energy. The resulting decay constants are 0.10, 0.51, 0.75, and 0.97 for thallium, as well as 0.21, 0.74, and 2.29 for silver. All decay constants are given in atomic units.

[51] H. J. Monkhorst and J. D. Pack, Special points for Brillouin-zone integrations, Phys. Rev. B **13**, 5188 (1976).

[52] L. Eschmann, A. Sabitova, R. Temirov, F. S. Tautz, P. Krüger, and M. Rohlfing, Coverage-dependent anisotropy of the NTCDA/Ag(111) interface state dispersion, Phys. Rev. B **100**, 125155 (2019).

[53] L. E. Davis, *Handbook of Auger Electron Spectroscopy: A Reference Book of Standard Data for Identification and Interpretation of Auger Electron Spectroscopy Data* (Physical Electronics Industries, 1976).

[54] M. P. Seah and W. A. Dench, Quantitative electron spectroscopy of surfaces: A standard data base for electron inelastic mean free paths in solids, Surf. Interface Anal. **1**, 2 (1979).

[55] S. Tanuma, C. J. Powell, and D. R. Penn, Calculations of electron inelastic mean free paths for 31 materials, Surf. Interface Anal. **11**, 577 (1988).

[56] S. Tanuma, C. J. Powell, and D. R. Penn, Calculations of electorn inelastic mean free paths. II. Data for 27 elements over the 50–2000 eV range, Surf. Interface Anal. **17**, 911 (1991).

[57] J. Coraux, T. N. Plasa, C. Busse, T. Michely *et al.*, Structure of epitaxial graphene on Ir (111), New J. Phys. **10**, 043033 (2008).

[58] K. J. Rawlings, M. J. Gibson, and P. J. Dobson, The epitaxial growth of lead and thallium on (111) silver and copper, J. Phys. D **11**, 2059 (1978).

[59] M. F. Toney, J. G. Gordon, M. G. Samant, G. L. Borges, O. R. Melroy, L.-S. Kau, D. G. Wiesler, D. Yee, and L. B. Sorensen, Surface x-ray-scattering measurements of the substrate-induced spatial modulation of an incommensurate adsorbed monolayer, Phys. Rev. B **42**, 5594 (1990).

[60] M. F. Toney, J. G. Gordon, M. G. Samant, G. L. Borges, O. R. Melroy, D. Yee, and L. B. Sorensen, Underpotentially deposited thallium on silver (111) by in situ surface x-ray scattering, Phys. Rev. B **45**, 9362 (1992).

[61] M. F. Toney, J. G. Gordon, M. G. Samant, G. L. Borges, O. R. Melroy, D. Yee, and L. B. Sorensen, In-Situ atomic structure of underpotentially deposited monolayers of Pb and Tl on Au(111) and Ag(111): A surface x-ray scattering study, J. Phys. Chem. **99**, 4733 (1995).

[62] M. Getzlaff, M. Bode, R. Pascal, and R. Wiesendanger, Adsorbates on Gd(0001): A combined scanning tunneling microscopy and photoemission study, Phys. Rev. B **59**, 8195 (1999).

[63] P.-J. Hsu, T. Mauerer, W. Wu, and M. Bode, Observation of a spin-density wave node on antiferromagnetic Cr(110) islands, Phys. Rev. B **87**, 115437 (2013).

[64] D. Carnal, P. I. Oden, U. Müller, E. Schmidt, and H. Siegenthaler, In-situ STM investigation of Tl and Pb underpotential deposition on chemically polished Ag (111) electrodes, Electrochim. Acta **40**, 1223 (1995).

[65] T. Wiederholt, H. Brune, J. Wintterlin, R. J. Behm, and G. Ertl, Formation of two-dimensional sulfide phases on Al(111): An STM study, Surf. Sci. **324**, 91 (1995).

[66] Th. Fauster, Quantization of electronic states on metal surfaces, Appl. Phys. A **59**, 479 (1994).

[67] P. M. Echenique and J. B. Pendry, Theory of image states at metal surfaces, Prog. Surf. Sci. **32**, 111 (1989).

[68] G. Binnig, K. H. Frank, H. Fuchs, N. Garcia, B. Reihl, H. Rohrer, F. Salvan, and A. R. Williams, Tunneling Spectroscopy and Inverse Photoemission: Image and Field States, Phys. Rev. Lett. **55**, 991 (1985).

[69] A. Kubetzka, M. Bode, and R. Wiesendanger, Spin-polarized scanning tunneling microscopy in field emission mode, Appl. Phys. Lett. **91**, 012508 (2007).

[70] S. R. Park, C. H. Kim, J. Yu, J. H. Han, and C. Kim, Orbital-Angular-Momentum Based Origin of Rashba-Type Surface Band Splitting, Phys. Rev. Lett. **107**, 156803 (2011).

[71] J. Wieferink, P. Krüger, and J. Pollmann, Improved hybrid algorithm with Gaussian basis sets and plane waves: First-principles calculations of ethylene adsorption on $\beta-$Si C(001)-(3×2), Phys. Rev. B **74**, 205311 (2006).